ARTICLE

Check for updates

Enhanced electrical conductivity and mechanical properties in thermally stable fine-grained copper wire

Qingzhong Mao[1], Yusheng Zhang[2], Yazhou Guo[3] & Yonghao Zhao[1✉]

The rapid development of high-speed rail requires copper contact wire that simultaneously possesses excellent electrical conductivity, thermal stability and mechanical properties. Unfortunately, these are generally mutually exclusive properties. Here, we demonstrate directional optimization of microstructure and overcome the strength-conductivity tradeoff in copper wire. We use rotary swaging to prepare copper wire with a fiber texture and long ultrafine grains aligned along the wire axis. The wire exhibits a high electrical conductivity of 97% of the international annealed copper standard (IACS), a yield strength of over 450 MPa, high impact and wear resistances, and thermal stability of up to 573 K for 1 h. Subsequent annealing enhances the conductivity to 103 % of IACS while maintaining a yield strength above 380 MPa. The long grains provide a channel for free electrons, while the low-angle grain boundaries between ultrafine grains block dislocation slip and crack propagation, and lower the ability for boundary migration.

[1] Nano and Heterogeneous Materials Center, School of Materials Science and Engineering, Nanjing University of Science and Technology, Nanjing, China.
[2] XI'AN Rare Metal Materials Institute Co.Ltd, Xi'an, China. [3] School of Aeronautics, Northwestern Polytechnical University, Xi'an, China.
✉email: yhzhao@njust.edu.cn

The appearances of the first train in the world developed by Richard Trevithick in 1803 and the first commercial railway from Darlington to Stockton at England in 1825 opened the new era of human transportation. Since the emerging of Shinkansen in Japan in 1964, high speed electric rail has been ushering in a new global development, as witnessed by its five-fold increase in the world's total mileage over the past two decades. Copper contact wire provides electric energy and traction power for high speed train, which is one of the most critical components affecting safety and reliability. The development trend of constantly increasing speed of high speed train proposes critical requirements for the contact wire, which must simultaneously possesses excellent electrical conductivity, mechanical properties and thermal stability. First, the continuous speed increase of high speed rail requires the contact wire to provide more current and tractive power, which will bring in overheat and spark-wear. To solve these problems, we have to enhance the conductivity of the contact wire. Second, high speed slide between pantograph (an equipment for electrified railway trains to obtain power from the contact wire), and the contact wire will activate shear wave of up and down vibration, which requires the good impact resistance and damage tolerance of the contact wire. Moreover, the increase in speed needs to further strengthen the contact wire because stable working condition between the pantograph and contact wire can be reached only when the running speed of trains is smaller than 70% velocity of shear wave V_c, and V_c is proportional with the square root of stringing tension T[1]: $V_c = 3.6(T/\rho)^{1/2}$, where ρ is density of contact wire. Therefore, only strengthening the contact wire can permit a high T, which further permits a high V_c and running speed of trains. Third, increase in running speed also requires high thermal stability and wear resistance.

Unfortunately, high strength and high conductivity as well as thermal stability are seldom co-existing simultaneously. Figure 1 compares relations of yield strength and conductivity as well as thermal stability of pure coarse-grained (CG) and ultrafine grained (UFG with grain size smaller than 1 μm) copper (Cu)[2–27]. First, yield strength and conductivity are always trade-off with each other (as shown by the dashed orange line for guidance)[2–18]. Conventional strengthening mechanisms including grain refinement and deformation[6–8,16] routinely enhance the yield strength with the expense of their conductivity (Fig. 1a). An exceptional data point (red circle) with an ultra-high yield strength of 980 MPa and conductivity of 97% of international annealed copper standard (IACS) was obtained in nano-twinned Cu prepared by pulse electro-deposition (ED)[11], and seems to escape from the area under the dash line. However, it basically follows the strength-conductivity trade-off rule because twin boundaries (TBs) still have low electron scattering effect[28,29]. The underlying mechanism for determining strength-conductivity trade-off dilemma is that grain boundaries (GBs) and dislocations for strengthening unavoidably introduce the lattice imperfections, which caused electron scattering. It seems that the conductivity of the CG Cu is the extreme limit, which is difficult to exceed.

Strength and thermal stability of UFG Cu are also consuming each other, as shown by the dashed orange line for guidance in Fig. 1b. The final grain size increases linearly with increasing annealing temperature[16,17,19–27], i.e., low annealing temperature corresponds to small grains, and on the other hand, the smaller the grain size, the lower the thermal stability. According to Hall–Petch relationship (yield strength is proportional to one over of square root of grain size), the higher the strength, the lower the thermal stability, namely strength-thermal stability paradox. The underlying mechanism is that both GBs and dislocations for strengthening simultaneously increase the free energy of the systems and provide driving force for GB migration.
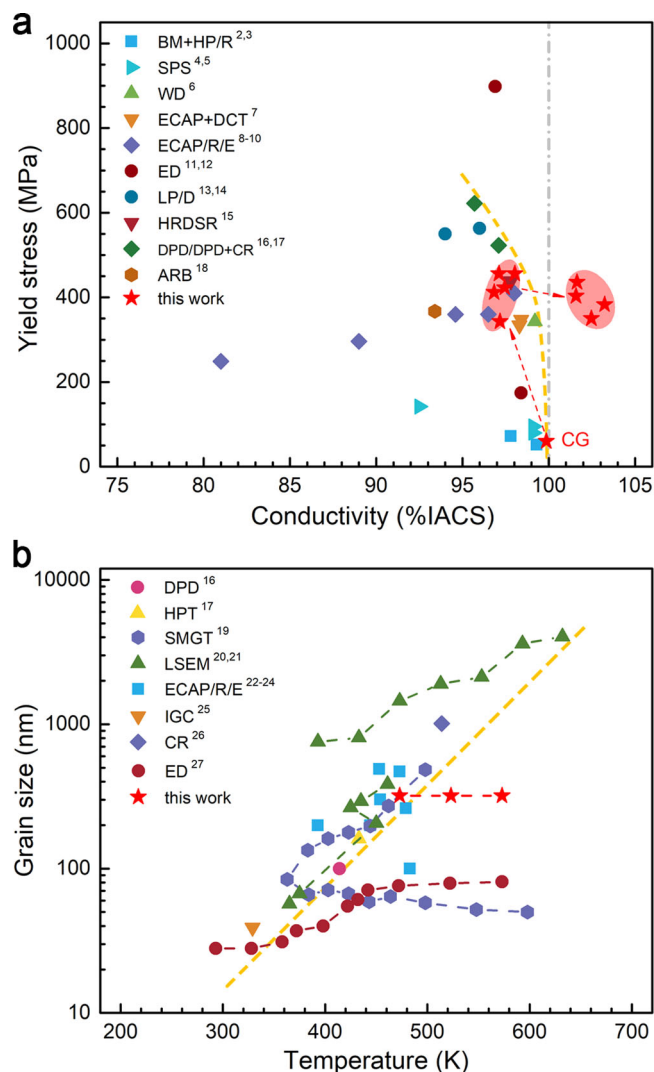

Fig. 1 Literature review for relations of yield strength and conductivity as well as thermal stability of pure CG and UFG copper prepared by different severe plastic deformation and powder sintering methods[2–27]. a Yield strength versus conductivity. b Grain size versus annealing temperature. BM ball milling, HP/R hot pressing and rolling, SPS spark plasma sintering, WD wire drawing, ECAP/R/E equal-channel angular pressing, rolling and extrusion, DCT deep cryogenic treatment, ED electro-deposition, LP/D liquid pressing and drawing, HRDSR high-speed-ratio differential speed rolling, DPD dynamic plastic deformation, CR cold rolling, ARB accumulative rolling bonding, SMGT surface mechanical grinding treatment, LSEM large strain extrusion machining, HPT high-pressure torsion, IGC inert gas condensation.

There are two cases deviated from the general rule for the nano-twinned Cu[27] and UFG Cu prepared by SMGT[19]. The relatively high thermal stability is explained by the low energies of TBs and low-angle GBs[27,30].

Strictly speaking, strength-conductivity paradox was not broken yet because all strengthening strategies no matter via twin boundaries, low angle grain boundaries or dislocations unexceptionally caused electron scattering, and enhancing strength and lowering conductivity are two parts of every lattice defect, like the two sides of a coin, we could not separate the head and the tail. However, the two sides of lattice defects do not deny yet the possibility of existence of some structures simultaneously beneficial to strength and conductivity. After all, strength and conduction are not exactly the same thing. The former is related
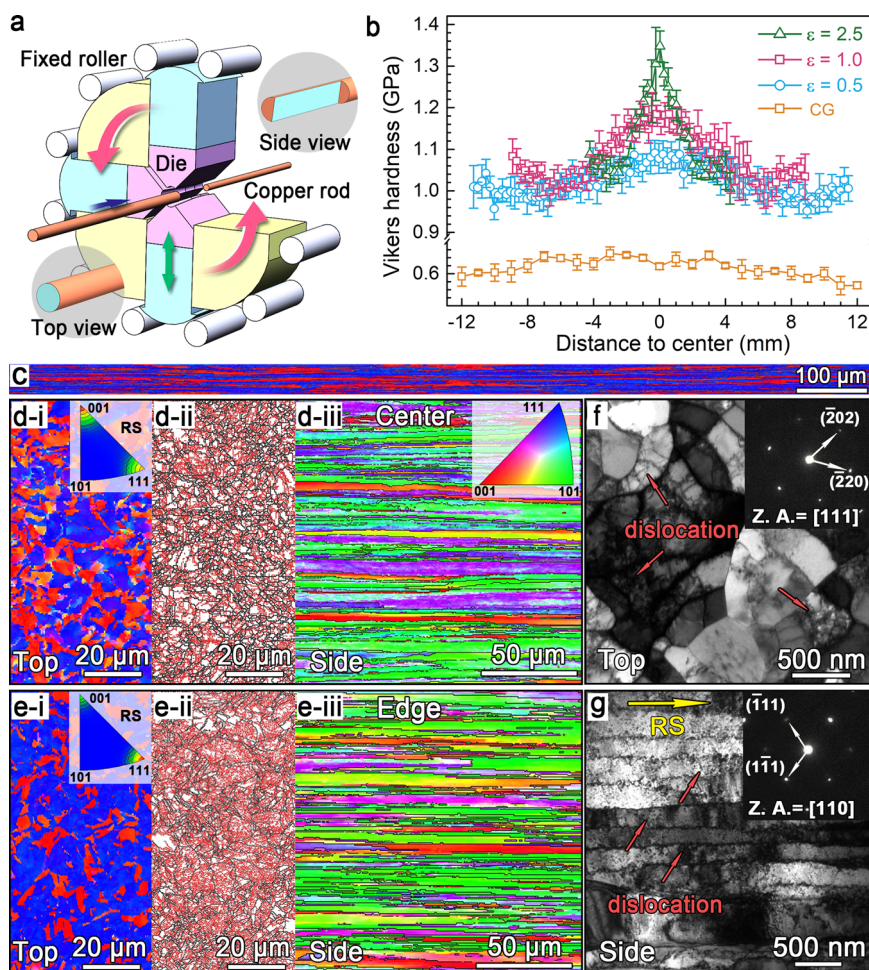
Fig. 2 Processing, micro-hardness and microstructures of the swaged copper. a Schematic illustration of rotary swaging technique. **b** Vickers micro-hardness measured from center to edge along the radial direction (the error bar represents the standard deviation of hardness). **c** EBSD crystal orientation map (filled with orientation information of cross section) with $\varepsilon = 2.5$. **d**, **e** EBSD crystal orientation maps and GB maps in the rod center (**d**-i, **d**-ii, **d**-iii) and at the edge (e-i, e-ii, e-iii) with $\varepsilon = 2.5$ from top (**d**-i, **d**-ii, **e**-i, and **e**-ii) and side (**d**-iii and **e**-iii) views. The insets are inverse pole figures and color code, respectively. Black and red lines in **d**-ii and **e**-ii represent high angle GBs (>15°) and low angle GBs between 2° and 15°, respectively. **f**, **g** TEM images of the swaged copper with $\varepsilon = 2.5$ from top (**g**) and side (**h**) views. The insets are selected area electron diffraction (SAED) patterns.

to dislocation behavior, while the latter is related to electron motion. In fact, we need a microstructure that only blocks dislocations and does not scatter electrons. Traditional solution in literature to solve properties paradox is to compromise among the exclusive properties via combining their corresponding favorable structures together. For instance, both moderate strength and ductility are achieved in bimodal and gradient nano-grained Cu, because UFG grains contribute to strength and CGs to ductility[31–33]. In fact, the compromise only makes a balance between the contradictory properties, does not solve the contradiction from the root. Here learning from nature, we found nearly all biological tissues are directionally optimized materials (DOM). For example, to avoid fracture, rod-shaped bone and tree trunk evolve into fiber structure. This inspires us to change our thinking to solve the contradiction from the biology concept. In this work, we optimized UFG grains along Cu wire axis to simultaneously achieve high strength and high conductivity (Fig. 1a) as well as high thermal stability (Fig. 1b).

Results

Microstructures of the swaged copper. An annealed as-received high-purity Cu rod (99.98%, Supplementary Table 1 and Supplementary Fig. 1) was rotary swaged (RS) at room temperature

(Fig. 2a). During swaging, four dies were evenly arranged in the circumference of the Cu rod, revolved around the rod at a high speed, and at the same time made high frequency short-range strokes along the radial direction. The Cu rod was then deformed under a high strain rate of approximately $1\,s^{-1}$ and a high hydrostatic stress from the die impacts (Supplementary Fig. 2 and Supplementary Table 2). A series of molds were used to gradually reduce the Cu diameter to true deformation strains ε of 0.5, 1.0, 1.5, 2.0, and 2.5, respectively.

As shown in Fig. 2b, the micro-hardness of the CG Cu is 0.6 GPa, and swaging process increases the overall micro-hardness over 1.0 GPa, and gradually forms peak shape distributions along the radial direction with the highest values in the center and low values at the edge. Moreover, the micro-hardness peak becomes sharper with increasing swaging strain. For the swaged Cu with $\varepsilon = 2.5$, the micro-hardness is 1.35 GPa in the center and it gradually decreases to 1.05 GPa at the edge. Every impact from the swaging die doesn't go around the Cu rod center, which leads to the maximum strain superposition and micro-hardness in the rod center (Supplementary Fig. 3). The surface roughness R_a of the swaged Cu rods decreases from 1.05 μm to 0.4 μm, as shown in Supplementary Fig. 4.

Electron backscattering diffraction (EBSD), transmission electron microscopy (TEM), and X-ray diffraction (XRD) analyses (Fig. 2c–g, Supplementary Tables 3–6, and Supplementary Figs. 5 and 6)

indicate the swaging process gradually introduces strong <111> and weak <100> fiber textures, dislocations, cell structures with low angle GBs into initial CGs, and their number first increases significantly and then tends to saturation or decreases slightly when $\varepsilon = 2.5$. As a result, the initial CG grains are refined along the radial direction (Fig. 2d-ii and e-ii) and elongated with an average length of 300 μm (Fig. 2c, d-iii and e-iii) along the axial direction. Moreover, low-angle GBs are dominant after rotary swaging, while high-angle GBs are dominant in CG Cu (Supplementary Table 5 and Supplementary Fig. 5). For example, the fraction of low-angle GBs at the rod center increases from 2.4% ($\varepsilon = 0.1$) to 72.9% ($\varepsilon = 0.5$) and decreases slightly to 64.2% ($\varepsilon = 2.5$), suggesting low angle GBs are dominant in the swaged Cu when $\varepsilon > 0.5$ (Supplementary Table 5). With increasing ε upto 2.5, the local misorientation distribution becomes broader and moves towards higher angle, suggesting the increase of dislocation density, which was quantitatively calculated in Supplementary Table 6. TEM observations (Fig. 2f, g) revealed that columnar dislocation cells with an average diameter of about 320 nm are aligned along the axis of the Cu rod with $\varepsilon = 2.5$. The boundaries between cells are low-angle GBs, as revealed by selected area electron diffraction (SAED) patterns in Fig. 2f, g, and there exist plenty of dislocations within the cells. The dislocation density was estimated from EBSD average local misorientation as about $9.19 \times 10^{14}\,\text{m}^{-2}$ (Supplementary Table 6). Moreover, gradient microstructures are revealed along the radial direction, and the above microstructural parameters increase from edge to center (Supplementary Fig. 5), explaining the corresponding variations of micro-hardness in Fig. 2b.

Mechanical properties of the swaged copper. To characterize mechanical properties of the swaged Cu, we performed quasi-static and dynamic tensile and compressive, Charpy impacting and wearing tests. Quasi-static tensile curves of the swaged Cu at room and liquid nitrogen (LN) temperatures are shown in Fig. 3a and Supplementary Figs. 7 and 8. The CG Cu has a yield strength of 60 MPa and tensile ductility of 57%. The swaging process gradually increases the yield strength up to 450 MPa and decreases the ductility down to 10% in the Cu rod center when $\varepsilon = 2.5$ (Fig. 3b). For the swaged Cu, necking occurs immediately after yielding because of nearly null strain hardening capability[31]. The swaging deformation consumed the strain hardening capability by saturating dislocation accumulation. Moreover, the yield strength increases from edge to center (Supplementary Figs. 7 and 8), agreeing with the micro-hardness variations. The poor ductility and strain hardening capability are improved when the sample was tested at LN temperature or annealed, due to the further enhanced dislocation accumulation capability (Fig. 3a)[31,34,35].

Charpy V-notch impact test was used to measure impact absorbed energy reflecting damage tolerance under impact. As shown in Fig. 3c, the impact absorbed energy of CG Cu is about 5 J, and it is enhanced gradually up to 9 J when $\varepsilon = 2.5$ and impacted from side. Scanning electron microscopy (SEM) and EBSD side views (Fig. 4a–i) revealed that the main crack of the swaged Cu is deviated severely and propagated in a zigzag way (Fig. 4f), and is accompanied with a large number of isolate lamellar cracks along GBs at the front of crack (Fig. 4e, f, h, i). The isolate micro-cracks and zigzag propagation of crack increase the fracture surface by absorbing more impact energy, as schematically represented by Supplementary Fig. 9. Evident grain refinement was found along crack of swaged Cu due to recrystallization caused by impact heat (Fig. 4f, i). In literature, a low alloy steel with similar ultrafine elongated grains was reported to have an enhanced impact energy (226 J) than its CG counterpart (14 J)[36]. However, equiaxed ultrafine grained Cu prepared by ECAP has similar impact energy with their CG Cu counterpart[37]. Due to the large grain aspect ratio,

we expect the impact absorbed energy of the swaged Cu along axis is much smaller than that along radial direction.

Dynamic compressive stress-strain curves of the CG and swaged Cu samples with strain rates from 1000 to 3000 s^{-1} are shown in Fig. 3d. The swaged Cu exhibits anisotropic impact behavior, when loading from top and side due to their anisotropic microstructures. The stress–strain curve impacted from top is higher than that from side. Moreover, there still exists slight strain hardening because dynamic impact caused further dislocation accumulation[38]. For all impacted Cu samples, no adiabatic shear bands (ASBs) are observed. ASBs originate from the sudden instability in the process of impact, which can cause catastrophic failure and engineering accidents. The adiabatic temperature rise of the swaged Cu is estimated to be smaller than 50 K, which is much smaller than $0.5T_{\text{m}}$ (melting point of Cu) and suggests thermal softening for ASBs could not occur (Supplementary Calculation 1)[39]. The susceptibility to ASBs χ_{ASB} was calculated as 35.8 for CG Cu and 2962.6 for the swaged Cu with $\varepsilon = 2.5$ (Supplementary Calculation 1), which are much smaller than ten thousands for ASBs in FCC metals[40]. In literature, ASBs are easy to happen in body centered cubic (BCC) and hexagonal close packed (HCP) metals and their UFG materials exacerbate ASBs[41,42]. Nevertheless, both CG and UFG FCC metals rarely produce ASBs due to their excellent deformability[38].

Figure 3e shows dynamic tensile stress-strain curves of the CG and swaged Cu samples with strain rates from 1000 to 3000 s^{-1}. The swaged Cu with $\varepsilon = 2.5$ have yield strength of above 500 MPa and 10% flat-form under a strain rate of 2000 s^{-1} due to enhanced dislocation accumulation[38]. Because the contact wire is subjected to the tests of stringing tension and vibration of shear wave in high-speed rail, the significantly enhanced yield strength and positive strain hardening of the swaged Cu can protect against rapid and premature necking instability. The higher yield strength of the swaged Cu under dynamic tension than that under dynamic compression might be due to their different cross-sectional areas of specimens cut from the rod center. The cross-sectional area of the dynamic tensile specimen (Ø3 mm) is smaller than that of the compressive one (5 × 5 mm). As shown in Fig. 2b, the closer to the center of the swaged rod, the higher the strength and hardness.

The contact wire used in high speed rail is subjected to high speed wear from the pantograph, therefore, its wear resistance is critically important property. The inset in Fig. 3f shows the variations of the friction coefficient (FC) of CG and swaged Cu against the sliding time. In the steady-state stage, FCs of CG and swaged Cu tend to a steady value of about 0.5. The wear rates of both CG and swaged Cu increase with increasing the load, as shown in Fig. 3f. Moreover, the swaged Cu exhibits much lower wear rates than those of the CG Cu counterpart, and anisotropic wear behavior with higher wear rate when wearing from side than that from top. SEM observation found that when wearing from side, the lamella grains were peeled off, while when wearing from top, the equiaxed ultrafine grains have more excellent wearing resistance (Supplementary Fig. 10). In literature, UFG materials are reported to have excellent wearing resistance due to their high hardness[43,44].

Thermal stability and conductivity of the swaged copper. The thermal stability of the swaged Cu is an essential property for potential engineering applications. Both isothermal and isochronal annealing were employed to characterize the thermal stability of the swaged Cu, as shown in Fig. 5a, b and Supplementary Fig. 11. The micro-hardness keeps at 1.25 GPa constantly when annealed at 473 K till 400 min, and slightly decreases
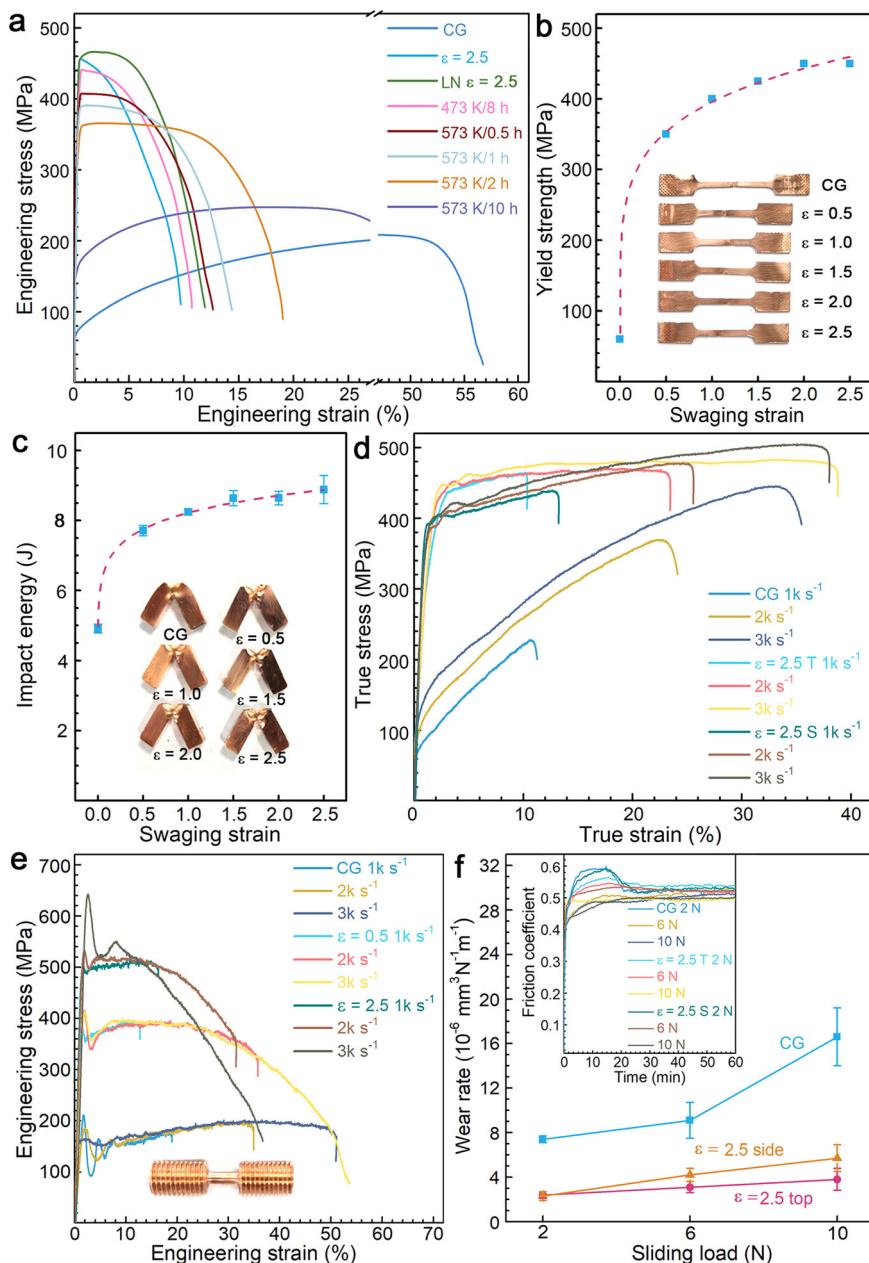
Fig. 3 Mechanical properties of the swaged copper in the center. a Quasi-static tensile curves of the swaged and CG copper tested at room and liquid nitrogen (LN) temperatures. **b** Yield strength versus swaging deformation stain. The insets are tensile fractured specimens. **c** Charpy absorbed impact energy vs swaging strain. The insets are fractured specimens (the error bar represents the standard deviation of impact energy). **d** Dynamic compressive curves with strain rates of 1000–3000 s⁻¹ loaded from top (T) and side (S), respectively. **e** Dynamic tensile curves with strain rates of 1000–3000 s⁻¹ loaded from top. **f** Wear rate and curves versus different sliding loads at room temperature loaded from top (T) and side (S). The inset is friction coefficient versus wearing time (the error bar represents the standard deviation of wear rate).

to 1.15 GPa when annealed at 523 K for 600 min due to dislocation recovery, as revealed by TEM images in Fig. 5c. Quantitative calculation also indicated that dislocation density is reduced by one order of magnitude after annealing (Supplementary Table 7). An evident and rapid drop of micro-hardness is observed when annealed at 573 K and recrystallization process appears at 120 min (Fig. 5c-iii). From Fig. 4b, when annealing time is 30 min, the micro-hardness can keep unchanged up to 473 K, and drops to 0.95 GPa at 623 K due to onset of recrystallization (Fig. 5c-iv).

Figure 1b compares our annealing results with literature data. Our data accompanied with two exceptional cases for the nano-twinned Cu[27] and UFG Cu[19] prepared by SMGT deviated

from the general rule, and exhibited high thermal stability. Thermodynamic calculation indicated that the lamellar grain structure has a lower stored energy due to the lower energy and volume fraction of low-angle GBs as compared with equiaxed grains (Supplementary Calculation 2)[23]. Kinetic calculation revealed that the swaged Cu has higher activation energy of recrystallization ($Q = 150$ J mol⁻¹ K⁻¹) as compared to equiaxed ultrafine grained Cu[24] (72 J mol⁻¹ K⁻¹) (Supplementary Calculation 3), which enhances thermal stability by retarding recrystallization process.

The conductivity of the swaged Cu is most critical property for applications. Four-point probe resistivity test at room temperature indicated that swaging process lowers the electrical
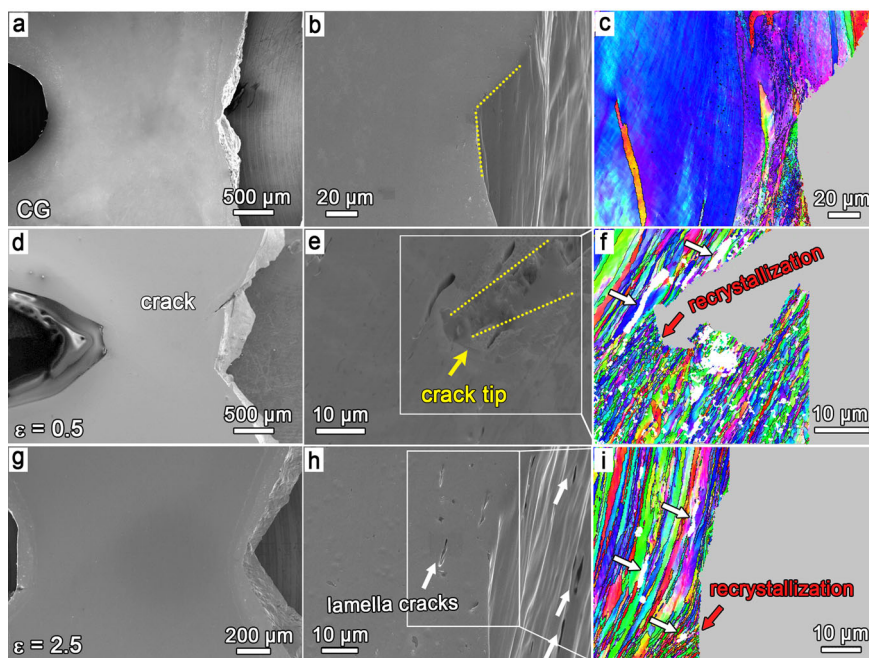
Fig. 4 Side-view SEM and EBSD images of the CG and swaged copper by Charpy V-notch impact at room temperature near the crack tip. a–c CG copper. **d–f** $\varepsilon = 0.5$. **h, i** $\varepsilon = 2.5$. Large number of isolate lamellar cracks along GBs at the front of main crack of the swaged copper was pointed out by white arrows in Fig. 4f, h, i.
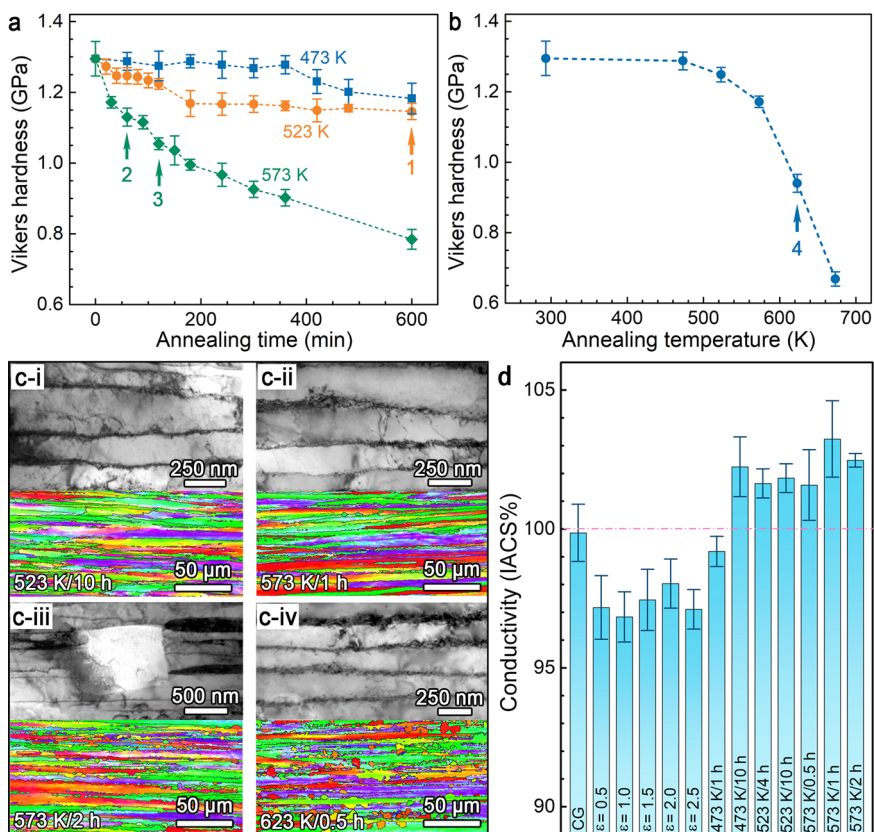

Fig. 5 Micro-hardness, microstructural evolutions and conductivity of the swaged copper with $\varepsilon = 2.5$ in the rod center during isothermal and isochronal annealing process. a Isothermal annealing at 473, 523, and 573 K (the error bar represents the standard deviation of hardness). **b** Isochronal annealing for 30 min at temperatures from 300 to 673 K (the error bar represents the standard deviation of hardness). **c** EBSD and TEM images of annealed side-view structure. **d** Conductivity of CG, swaged and annealed copper (the error bar represents the standard deviation of conductivity).
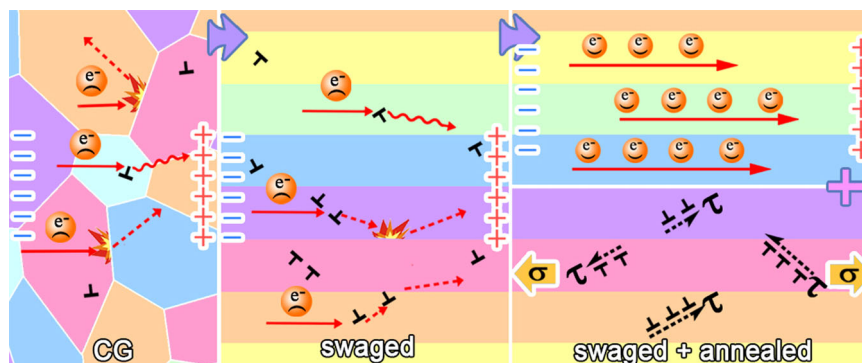
Fig. 6 Schematic representation of microstructural evolutions of copper during swaging and annealing processes and their influences on mechanical, thermal, and conductive properties. Electrons are mainly scattered by GBs and dislocations in the CG (figure in the right) and swaged copper (figure in the middle), respectively, while pass through the super-long oriented grain channels without scattering after annealing (figure in the upper right corner). The low-angle GBs with sub-micrometer interval block dislocation slip and enhance the strength (figure in the lower right corner).

conductivity of CG Cu from 100% to approximately 97% IACS due to the introduction of dislocations, etc. defects, which scatter free electrons as shown in Fig. 5. It is surprising that annealing at different temperatures for different times before recrystallization increases the conductivity of the swaged Cu over that of CG Cu and up to a highest value of 103% IACS, while still keeping the yield strength above 380 MPa. As shown in Fig. 1a, our data points break the limited boundary in conductivity of the CG Cu, representing a superior combination of strength and conductivity.

Discussion

Figure 6 schematically illustrated microstructural evolutions of Cu during swaging and annealing processes and their influences on mechanical, thermal, and conductive properties. First, for the CG Cu, high angle GBs are the main lattice imperfections that influence conductivity considering the low electron scattering effect of annealing TBs and extremely low dislocation density (figure in the left). Second, rotary swaging simultaneously introduced the super-long ultrafine grains along Cu wire axis and high density of dislocations in grain interiors. Although the super-long grains enhanced the conductivity by reducing the scattering effect from high angle GBs of CG Cu, the high density of dislocations on the electron passageway still lowers the conductivity down to about 97% IACS (figure in the middle). Third, most dislocations on the electron passageway were swept away after annealing prior to recrystallization and the conductivity was enhanced over 100% IACS (figure in the upper right corner). Finally, the low angle GBs with sub-micrometer interval increases the yield strength, impact, and wear resistance via effectively block dislocation slip on {111} planes and crack propagation in the radial direction (figure in the lower right corner). Moreover, the low energies of low angle GBs effectively lowered boundary migration ability along the radial direction from thermodynamic and kinetic points of view, thus increasing the thermal stability.

The commercial Cu contact wire used in electric rail with speed smaller than 200 km/h was prepared by drawing. It has an ultimate strength lower than 300 MPa and conductivity of 97.5% IACS[1]. Compared with the drawn Cu wire, the swaged Cu in the center has 50% increase in strength and comparable conductivity, and our swaged and annealed Cu has significantly enhanced conductivity still with 30% strength increase. Moreover, the swaging process of Cu wire has advantages of simple operation, low cost and high efficiency. As for the aspect of industrial applications, most preparation methods listed in Fig. 1 are expensive, complex, and inefficient, and their processed sample size is usually in the order of centimeter or even micrometer, being difficult to scale further up. In addition, solid solution and

precipitation strengthening were also used to develop the 2nd generation of Cu–Ag wire and 3rd generation of Cu–Mg and Cu–Sn wires used in electric rail with speeds between 200–300 km h^{-1}[45,46]. The 4th generation of Cu–Cr–Zr etc. alloys are still investigated in the laboratory to satisfy speeds larger than 350 km h^{-1} (Supplementary Fig. 12)[47]. Our present design concept provides a large space for above Cu alloys to further enhance their strength and conductivity. Moreover, our swaged Cu itself still has room for further strength improvement, for example, via low temperature rotary swaging to further refine ultrafine grains down to nanometer scale.

Although our DOM design achieved ultra-compatible conductive, mechanical, and thermal properties, and even broke strength-conductivity trade-off paradox in the axial direction of Cu wire, we haven't changed the laws of nature of strengthening mechanisms and electric conduction. The excellent conductivity in the axial direction comes at the expense of the conductivity in the radial direction. Therefore, the nature of our DOM design is to optimize the good performance of materials to the required place according to the actual working conditions and service environment, of course, this is at the cost of sacrificing the performance of other places. This tells us that we don't have to spend our energy to make perfect materials in all aspects, but to use steel on the blade.

Conclusions

In brief, we were inspired by the structural characteristics of directional optimization of biological tissues to prepare a Cu wire with microstructures optimized along wire axis by rotary swaging. The swaged Cu exhibit excellent thermal stability and mechanical properties of high strength, high resistances to V-notch impact, dynamic compression and tension as well as wear. Hundred and three percent of IACS conductivity, above that of the CG Cu counterpart, was achieved by subsequent annealing accompanying with the yield strength above 380 MPa. To the best of our knowledge, our work provides an alternative solution for properties trade-off paradox by directional optimization of microstructure. This is different from the conventional compromise of composite. Moreover, the swaging process of Cu wire has advantages of simple operation, low cost, and easy commercialization.

Methods

Materials, rotary swaging, and annealing processes. Fiber-textured ultra-fine grained Cu rods with purity of 99.98% were synthesized by means of rotary swaging at room temperature. The as-received Cu rods with a dimension of Ø30 mm × 2000 mm were first annealed at 973 K for 2 h under Ar atmosphere in order to produce a coarse-grained initial microstructure with an average grain size

7

of ~54 μm and free of texture. The annealed Cu bars were then rotary swaged at room temperature down to Ø23.4, 18.2, 14.2, 11.1, and 8.6 mm without inter-mediate annealing that corresponds to true deformation degrees $\varphi (= \ln(A_0/A)$, where A_0 and A are the initial and final cross-sectional areas) of 0.5, 1.0, 1.5, 2.0, and 2.5, respectively. The subsequent annealing process was performed in a furnace with N_2 gas as protecting atmosphere at 473, 523, 573, 623, and 673 K, respectively.

Vickers micro-hardness test. Vickers micro-hardness tests were performed using an HMV-G 21DT (Shimazdu, Japan) tester with a load of 0.98 N and a dwell time of 15 s. Sample surface was mechanically polished to be fresh, and ten indentations were tested to obtain reliable results.

Quasi-static uniaxial tensile test. Uniaxial tensile tests were performed using a LFM 20kN (walter + bai, Switzerland) tester with a strain rate of $1 \times 10^{-3}\,s^{-1}$ at room and liquid-nitrogen temperatures. The dog-bone-shaped tensile specimens with dimensions of $1 \times 3 \times 20\,mm^3$ were cut from the central position of swaged rods with gauge length along the swaging direction. Samples were clamped by hydraulic grips to avoid slippage during test. The strain was measured by using a standard non-contacting video extensometer. Three tensile specimens were tested to obtain reliable results.

Electrical conductivity test. The electrical conductivity test was performed using a four point probe resistivity tester at room temperature. The specimen has a dimension of $1 \times 1 \times 52\,mm^3$ with longitudinal direction parallel to the swaging direction. The specimens were strictly cut from the central positions of all rods. The value of conductivity σ is determined as follow:

$$\sigma = \frac{1}{\rho} = \frac{L}{RS}, \tag{1}$$

where ρ is the electrical resistivity, R is the resistance, S is the cross-sectional area and L is the length between two voltage probes.

Charpy impact test. The impact absorbed energy was measured by means of Charpy V-notch impact tests using a 15 J pendulum instrumented 50PH (walter + bai, Switzerland) tester at room temperature. The specimen has a dimension of $3 \times 4 \times 18\,mm^3$ with longitudinal direction parallel to the swaging direction. A 60° "V" groove was machined in the middle and the notch depth was 1 mm. The impact specimens were strictly cut from the central positions of all rods. At least three successful measurements were performed.

Dynamic tensile and compressive impacts. The split Hopkinson pressure bar (SHPB) setup locates at Northwestern Polytechnical University, Xi'an. The lengths of the input bar and output bar are 1500 mm and 1500 mm, respectively. Their diameters, together with the striker bar, are all 12.7 mm. The length of the striker bar varies from 350 to 600 mm to get appropriate strain rate and deformation. A copper disc with a diameter of 3 mm is used as pulse shaper. The thickness of the disc varies according to the loading rates. The input pulse shape is controlled to ensure stress equilibration within the specimen. Another function of the pulse shaper is to achieve constant strain rate during loading. Specimens with dimensions of Ø3 × 6 mm² for tension and $5 \times 5 \times 5\,mm^3$ for compression were cut from the central region of swaged Cu rods. The tensile impact loading direction was parallel to the swaging direction, and the compressive impact loading directions were parallel and vertical to the swaging direction. The average impact strains are ~1000, 2000, and 3000 s^{-1}, respectively. The strain rate $\dot{\varepsilon}(t)$, strain $\varepsilon(t)$ and stress $\sigma(t)$ of the specimen during dynamic Hopkinson compressive impact can be derived from incident, reflecting and transmitting strain $\varepsilon_I(t)$, $\varepsilon_R(t)$, and $\varepsilon_T(t)$, which can be measured by strain extensometers attached on the incident and transmitted bars:

$$\dot{\varepsilon}(t) = \frac{C_0}{L}[\varepsilon_I(t) - \varepsilon_R(t) - \varepsilon_T(t)], \tag{2}$$

$$\varepsilon(t) = \frac{C_0}{L}\int_0^t [\varepsilon_I(t) - \varepsilon_R(t) - \varepsilon_T(t)]dt, \tag{3}$$

$$\sigma(t) = \frac{AE}{2A_0}[\varepsilon_I(t) + \varepsilon_R(t) + \varepsilon_T(t)], \tag{4}$$

where C_0, A, and E are the wave velocity, cross sectional area and elasticity modulus of input bar, respectively. A_0 and L are the initial cross-sectional area and length of sample.

Friction and wear tests. Sliding tests of the Cu samples were performed on a Bruker UMT-TriboLab testers in a ball-on-plate contact configuration under dry condition at room temperature in air with a relative humidity of 50 ± 5%. Balls of 6 mm in diameter were made of WC-Co with a micro-hardness of 17.5 GPa. Before sliding tests, the three kinds of Cu samples were electrochemically polished to the same level of surface roughness (Ra ~ 0.03 μm). The tests were carried out at a sliding stroke of 2 mm, a sliding velocity of 10 mm s^{-1}, and normal loads of 2, 6, and 10 N. One sliding cycle is defined as two strokes. Friction coefficient $\mu = F/P$,

where F is frictional force and P is normal applied load. μ values were recorded automatically.

Microstructure observations. X-ray diffraction (XRD) measurements were performed on a Bruker-AXS D8 diffractometer with Cu Kα radiation. The 2θ angle ranged from 40 to 100° and the scanning speed was 6° min^{-1}.

Electron backscattered diffraction (EBSD) analysis was performed on a Zeiss Auriga focused ion beam and scanning electron microscope equipped with a fully automatic Oxford Instruments Aztec 2.0 EBSD system (Channel 5 Software). EBSD sample surfaces were grinded to mirror-like condition and then electro-polished using 2.1 V dc in 85% H_3PO_4 + 15% deionized water to remove micro-scratches and relax strained layers. The scanning step size and accelerate voltage were 200 nm and 15 kV, respectively. The fracture surfaces of specimens were also examined by scanning electron microscopy (SEM) integrated in Zeiss Auriga.

The microstructures of the swaged Cu before and after annealing were examined by a TECNAI G2 20 LaB6 transmission electron microscope (TEM) operating at 200 kV. TEM foils were sliced by electrical spark machine and mechanically polished to a final thickness of about 40 μm, and then thinned by twin-jet polishing in an electrolyte of phosphoric acid (25%), alcohol (25%), and deionized water (50%) at about −10 °C.

Data availability
The raw data generated during this study are available from the corresponding author on reasonable request.

References
1. Huang, C. Q. On contact wire line used in catenary of high speed wheel-rail electrified railway. *China Railw. Sci.* **22**, 1–5 (2001).
2. Cao, M. et al. Aligning graphene in bulk copper: Nacre-inspired nanolaminated architecture coupled with in-situ processing for enhanced mechanical properties and high electrical conductivity. *Carbon* **117**, 65–74 (2017).
3. Chen, Y. et al. Fabrication of in-situ grown graphene reinforced cu matrix composites. *Sci. Rep.* **6**, 19363 (2016).
4. Jiang, R., Zhou, X., Fang, Q. & Liu, Z. Copper–graphene bulk composites with homogeneous graphene dispersion and enhanced mechanical properties. *Mater. Sci. Eng. A* **654**, 124–130 (2016).
5. Jiang, R., Zhou, X. & Liu, Z. Electroless ni-plated graphene for tensile strength enhancement of copper. *Mater. Sci. Eng. A* **679**, 323–328 (2017).
6. Joo, H. S., Hwang, S. K., Kim, Y. N. & Im, Y. T. Effect of continuous hybrid process on mechanical and electrical properties of rectangular pure copper wire. *J. Mater. Process. Technol.* **244**, 51–61 (2017).
7. Wei, K. X. et al. Effect of deep cryogenic treatment on microstructure and properties of pure copper processed by equal channel angular pressing. *Adv. Eng. Mater.* **21**, 1801372 (2019).
8. Habibi, A. & Ketabchi, M. Enhanced properties of nano-grained pure copper by equal channel angular rolling and post-annealing. *Mater. Des.* **34**, 483–487 (2012).
9. Habibi, A., Ketabchi, M. & Eskandarzadeh, M. Nano-grained pure copper with high-strength and high-conductivity produced by equal channel angular rolling process. *J. Mater. Process. Technol.* **211**, 1085–1090 (2011).
10. Higuera-Cobos, O. F. & Cabrera, J. M. Mechanical, microstructural and electrical evolution of commercially pure copper processed by equal channel angular extrusion. *Mater. Sci. Eng. A* **571**, 103–114 (2013).
11. Lu, L., Shen, Y., Chen, X., Qian, L. & Lu, K. Ultrahigh strength and high electrical conductivity in copper. *Science* **304**, 422–426 (2004).
12. Huang, G. et al. Preparation and characterization of the graphene-cu composite film by electrodeposition process. *Microelectron. Eng.* **157**, 7–12 (2016).
13. Bettinali, L., Tosti, S. & Pizzuto, A. Mechanical and electrical properties of cryo-worked cu. *J. Low Temp. Phys.* **174**, 64–75 (2013).
14. Han, K. et al. High strength and high electrical conductivity bulk cu. *Philos. Mag.* **84**, 3705–3716 (2004).
15. Kim, W. J., Lee, K. E. & Choi, S. H. Mechanical properties and microstructure of ultra fine-grained copper prepared by a high-speed-ratio differential speed rolling. *Mater. Sci. Eng. A* **506**, 71–79 (2009).
16. Zhang, Y., Li, Y. S., Tao, N. R. & Lu, K. High strength and high electrical conductivity in bulk nanograined cu embedded with nanoscale twins. *Appl. Phys. Lett.* **91**, 211901 (2007).
17. Zhang, Y., Tao, N. R. & Lu, K. Mechanical properties and rolling behaviors of nano-grained copper with embedded nano-twin bundles. *Acta Mater.* **56**, 2429–2440 (2008).

18. Takata, N., Lee, S. H. & Tsuji, N. Ultrafine grained copper alloy sheets having both high strength and high electric conductivity. *Mater. Lett.* **63**, 1757–1760 (2009).

19. Zhou, X., Li, X. Y. & Lu, K. Enhanced thermal stability of nanograined metals below a critical grain size. *Science* **360**, 526–530 (2018).

20. Saldana, C., King, A. H. & Chandrasekar, S. Thermal stability and strength of deformation microstructures in pure copper. *Acta Mater.* **60**, 4107–4116 (2012).

21. Wu, B., Chen, B., Zou, Z., Liao, S. & Deng, W. Thermal stability of ultrafine grained pure copper prepared by large strain extrusion machining. *Metals* **8**, 381 (2018).

22. Zhang, Y., Wang, J. T., Cheng, C. & Liu, J. Stored energy and recrystallization temperature in high purity copper after equal channel angular pressing. *J. Mater. Sci.* **43**, 7326–7330 (2008).

23. Liang, N. et al. Influence of microstructure on thermal stability of ultrafine-grained cu processed by equal channel angular pressing. *J. Mater. Sci.* **53**, 13173–13185 (2018).

24. Jenei, P., Gubicza, J., Yoon, E. Y., Kim, H. S. & Lábár, J. L. High temperature thermal stability of pure copper and copper–carbon nanotube composites consolidated by high pressure torsion. *Compos. Part A* **51**, 71–79 (2013).

25. Kumpmann, A., Günther, B. & Kunze, H. D. Thermal stability of ultrafine-grained metals and alloys. *Mater. Sci. Eng. A* **168**, 165–169 (1993).

26. Mao, Z. N. et al. Effect of equal channel angular pressing on the thermal-annealing-induced microstructure and texture evolution of cold-rolled copper. *Mater. Sci. Eng. A* **674**, 186–192 (2016).

27. Lu, L., Tao, N. R., Wang, L. B., Ding, B. Z. & Lu, K. Grain growth and strain release in nanocrystalline copper. *J. Appl. Phys.* **89**, 6408–6414 (2001).

28. Andrews, P. V., West, M. B. & Robeson, C. R. The effect of grain boundaries on the electrical resistivity of polycrystalline copper and aluminium. *Philos. Mag.* **19**, 887–898 (1969).

29. Callister, W. D. *Materials Science and Engineering: An Introduction* 7th edn, 674–676 (Wiley, 2007).

30. Liu, X. C., Zhang, H. W. & Lu, K. Strain-induced ultrahard and ultrastable nanolaminated structure in nickel. *Science* **342**, 337–340 (2013).

31. Wang, Y., Chen, M., Zhou, F. & Ma, E. High tensile ductility in a nanostructured metal. *Nature* **419**, 912–915 (2002).

32. Lu, K. Nanomaterials. Making strong nanomaterials ductile with gradients. *Science* **345**, 1455–1456 (2014).

33. Fang, T. H., Li, W. L., Tao, N. R. & Lu, K. Revealing extraordinary intrinsic tensile plasticity in gradient nano-grained copper. *Science* **331**, 1587–1590 (2011).

34. Wang, Y. M., Ma, E., Valiev, R. Z. & Zhu, Y. T. Tough nanostructured metals at cryogenic temperatures. *Adv. Mater.* **16**, 328–331 (2004).

35. Huang, X., Hansen, N. & Tsuji, N. Hardening by annealing and softening by deformation in nanostructured metals. *Science* **312**, 249–251 (2006).

36. Kimura, Y., Inoue, T., Yin, F. & Tsuzaki, K. Inverse temperature dependence of toughness in an ultrafine grain-structure steel. *Science* **320**, 1057–1060 (2008).

37. Liang, N., Zhao, Y., Wang, J. & Zhu, Y. Effect of grain structure on charpy impact behavior of copper. *Sci. Rep.* **7**, 44783 (2017).

38. Cheng, S. et al. High plasticity and substantial deformation in nanocrystalline nife alloys under dynamic loading. *Adv. Mater.* **21**, 5001–5004 (2009).

39. Liu, S. et al. Microstructural softening induced adiabatic shear banding in ti-23nb-0.7ta-2zr-o gum metal. *J. Mater. Sci. Technol.* **54**, 31–39 (2020).

40. Li, J. et al. Adiabatic shear localization in nanostructured face centered cubic metals under uniaxial compression. *Mater. Des.* **105**, 262–267 (2016).

41. Wei, Q. et al. Adiabatic shear banding in ultrafine-grained fe processed by severe plastic deformation. *Acta Mater.* **52**, 1859–1869 (2004).

42. Rittel, D. & Wang, Z. G. Thermo-mechanical aspects of adiabatic shear failure of am50 and ti6al4v alloys. *Mech. Mater.* **40**, 629–635 (2008).

43. Chen, X., Han, Z., Li, X. & Lu, K. Lowering coefficient of friction in cu alloys with stable gradient nanostructures. *Sci. Adv.* **2**, e1601942 (2016).

44. Curry, J. F. et al. Achieving ultralow wear with stable nanocrystalline metals. *Adv. Mater.* **30**, e1802026 (2018).

45. Huang, C. Q. Development of contact wire (trolley wire) for electric traction in China. *China Railw. Sci.* **24**, 61–65 (2003).

46. Yan, M., Wu, Y. C., Chen, J. C. & Zhou, X. L. Microstructure evolution in preparation of Cu-Sn contact wire for highspeed railway. *Adv. Mater. Res.* **415**, 446–451 (2012).

47. Liu, Q., Zhang, X., Ge, Y., Wang, J. & Cui, J. Z. Effect of processing and heat treatment on behavior of Cu-Cr-Zr alloys to railway contact wire. *Metall. Mater. Trans. A* **37**, 3233–3238 (2006).

Author contributions

Conceptualization, Y. H. Zhao; methodology, resources and material preparation, Q. Z. Mao; investigation and microstructural characterization, Q. Z. Mao, Y. S. Zhang, Y. Z. Guo; data curation, Q. Z. Mao; writing, supervision, project administration and funding acquisition, Y. H. Zhao; All authors have read and agreed to the published version of the manuscript.

Competing interests

The authors declare no competing interests.

Additional information

Supplementary information The online version contains supplementary material available at https://doi.org/10.1038/s43246-021-00150-1.

Correspondence and requests for materials should be addressed to Y.Z.

Peer review information Primary handling editors: Xiaoyan Li, John Plummer.

Reprints and permission information is available at http://www.nature.com/reprints

Publisher's note Springer Nature remains neutral with regard to jurisdictional claims in published maps and institutional affiliations.